Isolation of swarm sources using InSAR: the case of the February 2017 seismic swarm in western Anatolia (Turkey)

Nikos Svigkas [1,2] Simone Atzori,[2] Anastasia Kiratzi,[1] Cristiano Tolomei[2] and Stefano Salvi[2]

[1]*Aristotle University of Thessaloniki, Department of Geophysics, Thessaloniki, Greece. E-mail: svigkas@geo.auth.gr*
[2]*Istituto Nazionale di Geofisica e Vulcanologia, Osservatorio Nazionale Terremoti, Roma, Italia*

SUMMARY

We study the surface deformation of a moderate size $M5+$ earthquake swarm-type activity which burst at the tip of the Biga peninsula (western Turkey) in early 2017. No previous $M5+$ earthquakes have been recorded in the instrumental period on land, however, offshore normal faults, have ruptured to produce strong ($M > 6$) earthquakes. We use the Interferometric Synthetic Aperture Radar (InSAR) technique and exploit a data set of Sentinel-1 and ALOS-2 images, to successfully detect the surface deformation caused by three $M5+$ events of the sequence and constrain their source models, furtherly strengthened by seismic waveform analysis. The sequence occurred at shallow depths (<12 km) and is related with the activation of a normal fault. Our geodetic inversions constrained the rupture distribution of the main events and led us to conclude that they belong to a single fault plane, striking N110°E and dipping $\sim$40° to the SW, compatible with the regional tectonics. Furthermore, the InSAR analysis revealed that no aseismic transients occurred during the Biga swarm. InSAR applications in seismic swarms are limited mainly due to the low displacement signal they produce, which is not always easily detectable by radar satellites. Another obstacle is the time frequency of radar satellites acquisitions that often does not allow the temporal isolation of distinct seismic events. However, here we present a study that exploits InSAR data to isolate seismic sources of a swarm and proposes its use for the understanding of shallow seismic swarms in a systematic manner.

Key words: Geodetic instrumentation; Radar interferometry; Satellite geodesy; Seismicity and tectonics.

1 INTRODUCTION

InSAR investigations of strong seismic events have relatively recently started to be a systematic tool for the study of their displacement pattern. On the contrary, there are very few studies in the bibliography that have implemented it as a tool for studying seismic swarms; for the swarms occurring globally, in most of the cases, there is a complete absence of InSAR studies.

During the first 3 months of 2017, a shallow earthquake swarm of moderate magnitude $M5+$, occurred at the tip of the Biga peninsula (Fig. 1), in western Anatolia (Turkey). The sequence, also called the Ayvacik (Çanakkale) swarm, was characterized by the occurrence of more than 1500 events by the end of March 2017 (Fig. 2). The good coverage by the regional seismic networks (Fig. S1) enabled the analysis of seismicity down to magnitude 2 and even below. Although the number of reported injuries was small, some locals were placed in tents to reduce the risk of injury from collapsing buildings in consequent events. The strongest $M5+$ events caused damage to $\sim$2600 poorly constructed structures in 30 nearby villages, as reported by the field survey carried out after their occurrence (Livaoğlu *et al.* 2018).

The stress field in the broader region combines shearing and extension, placing the tip of the Biga peninsula in an active transtentional tectonic regime (e.g. Chatzipetros *et al.* 2013; Bulut *et al.* 2018). Shearing is imposed by the activity of the dextral strike-slip North Anatolian Fault (NAF) and its middle and southern strands (Fig. 1,e.g. Şengör 1979; Şengör *et al.* 2005; Özalp *et al.* 2013). The southern shore of the peninsula is controlled by the southern strand, where the dominant structure is the Edremit Fault Zone (EFZ, Sözbilir *et al.* 2016 and references therein). The strongest seismic event recorded at EFZ, within the instrumental period, is the 6 October 1944, M_w 6.8 Edremit-Ayvacik earthquake (Ambraseys 1988; Fig. 1), with a normal south-dipping source (dip $\sim$46°, e.g. Paradeisopoulou *et al.* 2010) which caused 73 fatalities, 275 injuries and over 2000 building failures (Altinok *et al.* 2012).
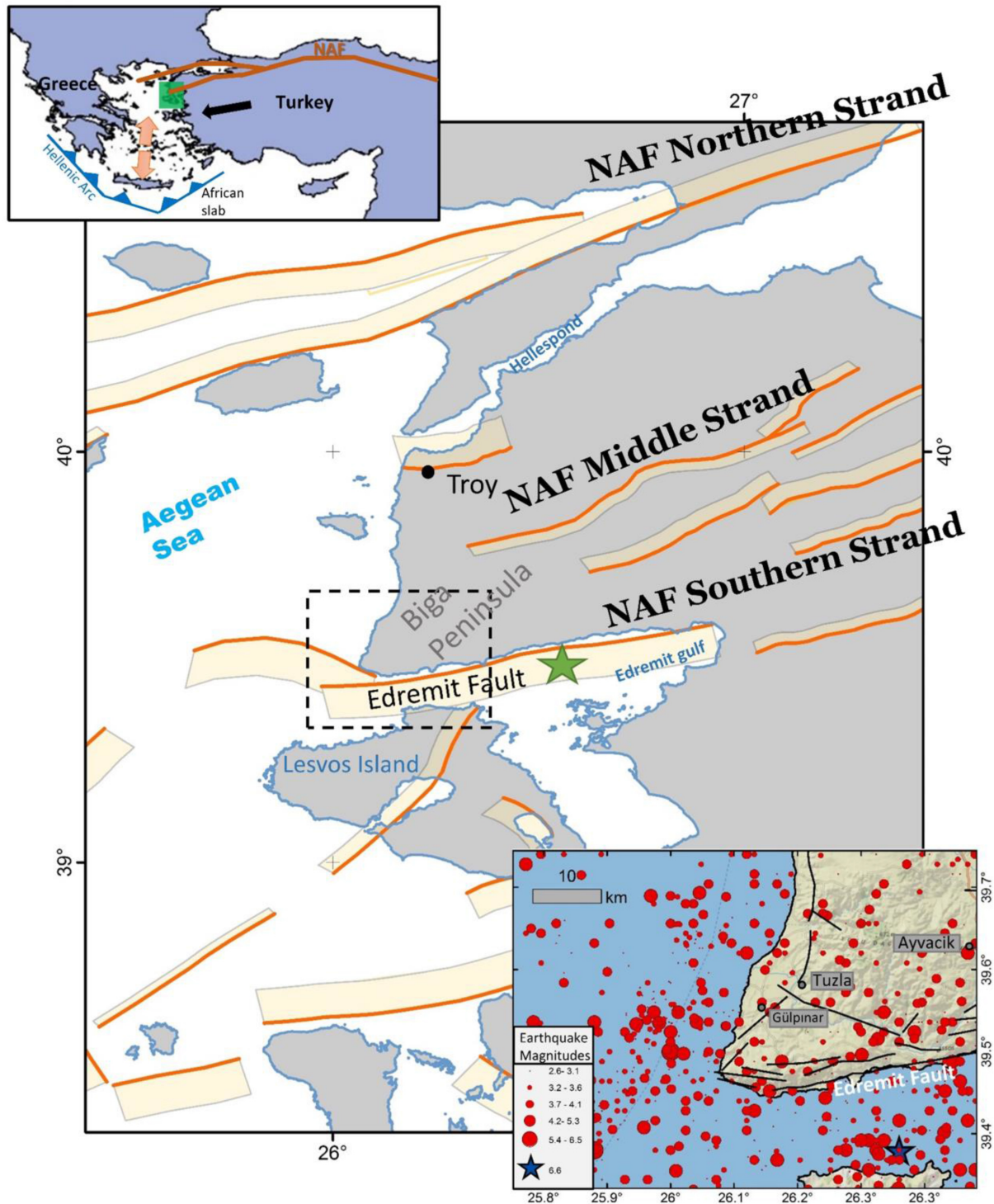
Figure 1. Location of the study area (dashed rectangle) in the broader tectonic framework of the North Anatolian Fault Zone (NAFZ). The orange polygons depict seismogenic sources (from the GreDaSS fault database) (Caputo & Pavlides 2013; Pavlides *et al.* 2010; Sboras 2012): lines denote the fault-top trace, whereas the transparent polygons show the fault dipping plane. The green star on Edremit fault marks the location of the 1944 earthquake. Upper left inset: location of the study area (green square) in a regional framework. Lower right inset: close-up on the area of study, with the local fault network (black lines, after Yılmaz & Karacık 2001). The geothermal power plant is located in Tuzla (coordinates 39.566066°N, 26.173216°E). The seismicity (red dots) is sparse on the Biga peninsula, but strong $M \geq 6.0$ events are mainly observed offshore (the data span the period 1300–2016).

The tip of Biga peninsula exhibits generally moderate-size seismicity; no $M > 5$ earthquakes occurred during instrumental period and no strong $M > 6$–7 during historical times. The site hosts important geothermal fields (e.g. Şamilgil 1966; Mützenberg 1997; Baba & Ertekin 2007; Şanlıyüksel & Baba 2007) which have been exploited since the ancient times. The seismic sequence occurred near to the Tuzla Geothermal Field (Baba *et al.* 2008, 2015), where a geothermal power plant, has been operating since
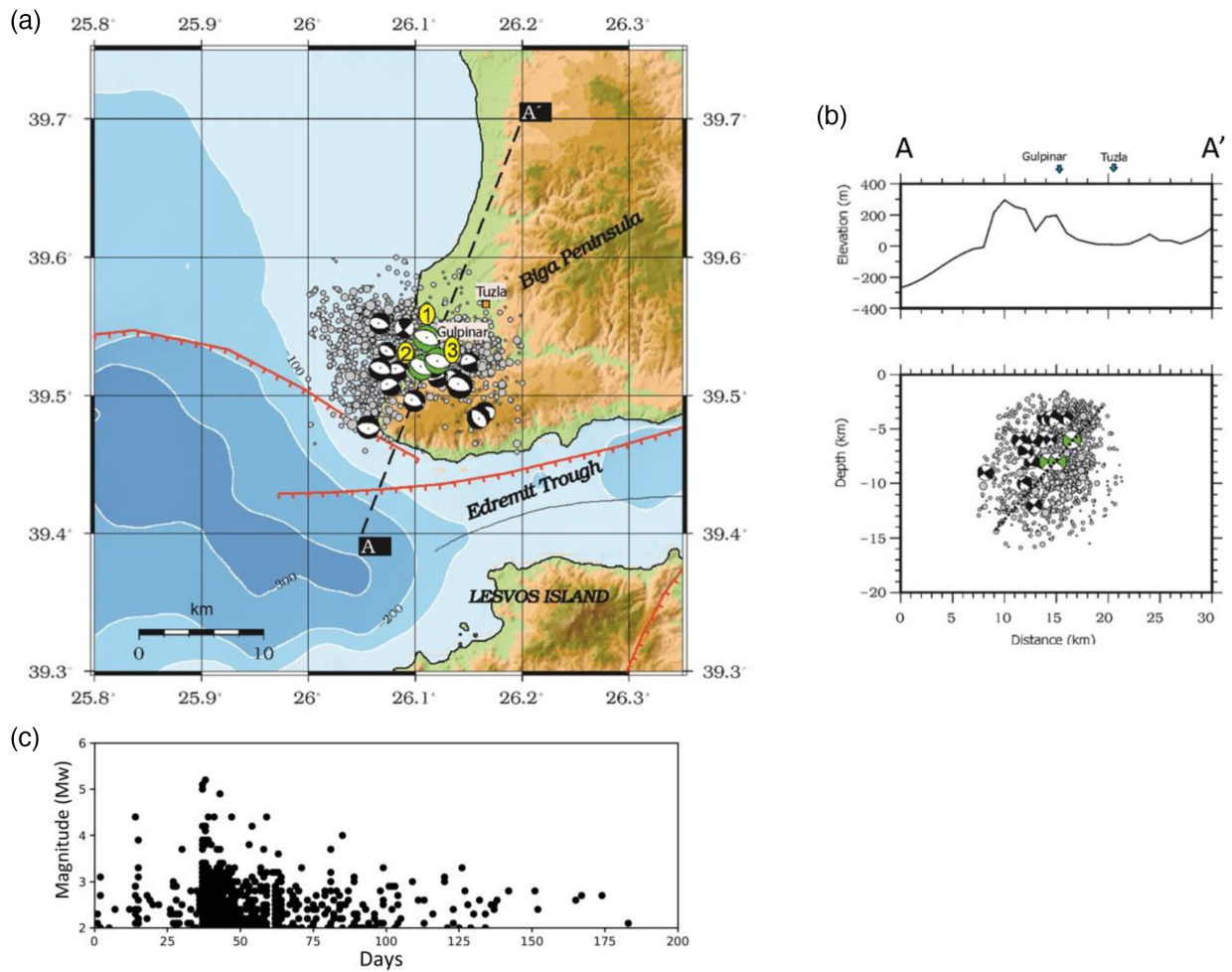
Figure 2. (a) Swarm activity (grey circles) at Biga peninsula, for the period 1/Jan/2017 to 30/Aug/2017. Green beach balls denote the moment tensor (MT) solutions of the three *M*5+ events that are analysed in this study using InSAR (numbered 1–3). Black beach balls depict other published MT solutions of the swarm (listed in Table S1). Normal faulting along WNW–ESE striking planes is well-depicted. The red lines denote faults (Caputo & Pavlides 2013; Pavlides *et al*. 2010; Sboras 2012). (b) Cross-section along dip, profile A–A' depicted in (a). The approximate location of the Gülpınar and Tuzla villages is marked. The dashed line passing through the projection of the three major events (green beach-balls) supports the assumption that the swarm is due to the activation of a SW dipping normal fault, located below these villages. (c) Magnitude–Time graph showing the evolution of the sequence.

2010. It is well accepted that in the presence of migrating fluids, fluid pore pressure variations might be the driving mechanism or at least facilitate the occurrence of swarm-type activity. The connection between the swarm occurrence and geothermal activity is not clear, and this investigation is outside the scope of this work.

Studies on swarm surface displacements are very limited and only recently, after the advent of space geodetic techniques, have been made available (Lohman & McGuire 2007; Bell *et al.* 2012; Kyriakopoulos *et al.* 2013, among others). Swarms often leave a weak surface signal that in many cases cannot be detected by radar satellites. This difficulty is the main reason for the lack of InSAR swarm studies in the existing bibliography. Even though the shorter satellite revisit times of Sentinel-1 have created more opportunities in terms of the ability to isolate specific seismic events, in many cases, it is still difficult to isolate all earthquakes. In most cases there will usually be a signal related to rapid afterslip (Elliott *et al.* 2016) and in some cases even strong post-seismic components.

This a basic disadvantage of InSAR compared to the high temporal resolution that seismic data can offer.

In this study, we detected displacement patterns associated with three main events of the 2017 Biga swarm. Using Differential InSAR (e.g. Zebker & Goldstein 1986; Dixon 1994; Massonnet 1997; Massonnet & Feigl 1998) we analysed three *M*5+events, hereinafter referred to as Event 1, 2 and 3 (Table 1). We exploited the revisit time of the Sentinel-1 A and B radar sensors and by applying an ad hoc modelling strategy, were able to estimate the slip distribution of all three *M*5+ events separately, while proposing fault segmentation for the swarm activity. Additionally, using Sentinel-1 and ALOS-2 data, we model the detected cumulative displace to find the cumulative slip distribution. The results of geodetic modelling are also compared with the sources and slip distributions obtained from the inversion of regional seismic data. Eventually, InSAR results are exploited to investigate the on-fault Coulomb Stress Changes and the possible interaction between the source of the 2017 swarm and the Edremit Fault.

Table 1. Combination of SLC images used in the study and the seismic events they contain.

Interferogram no.	Master image date	Master image time	Satellite of master image	Slave image date	Slave image time	Satellite of slave image	Satellite pass	Incidence angle (°)	Satellite look direction	Seismic events contained
1	20170125	04:14:47	Sentinel-1A (TOPS)	20170206	04:14:47	Sentinel-1A (TOPS)	Descending	43.88	*Right*	*Event 1:* 06 FEB 2017 03:51:40.7 Depth: 6 km M_w 5.3
2	20170131	04:14:04	Sentinel-1B (TOPS)	20170206	04:14:47	Sentinel-1A (TOPS)	Descending	43.84	*Right*	
3	20170206	16:06:23	Sentinel-1B (TOPS)	20170212	16:07:09	Sentinel-1A (TOPS)	Ascending	37.77	*Right*	*Event 3:* 07 FEB 2017 02:24:04.0 Depth: 8 km M_w 5.3
4	20170125	16:06:23	Sentinel-1B (TOPS)	20170206	16:06:23	Sentinel-1B (TOPS)	Ascending	37.77	*Right*	*Event 1:* 06 FEB 2017 03:51:40.7 Depth: 6 km M_w 5.3 *Event 2:* 06 FEB 2017 10:58:02.2 Depth: 8 km M_w 5.1
5	20170131	16:07:09	Sentinel-1A (TOPS)	20170212	16:07:09	Sentinel-1A (TOPS)	Ascending	33.94	*Right*	
6	20170106	04:22:48	Sentinel-1A (TOPS)	20170223	04:22:48	Sentinel-1A (TOPS)	Descending	33.85	*Right*	*Event 1:* 06 FEB 2017 03:51:40.7 Depth: 6 km M_w 5.3 *Event 2:* 06 FEB 2017 10:58:02.2 Depth: 8 km M_w 5.1
7	20161202	22:04:00	ALOS-2 (StripMap)	20170210	22:03:59	ALOS-2 (StripMap)	Ascending	31.41	*Right*	*Event 3:* 07 FEB 2017 02:24:04.0 Depth: 8 km M_w 5.3
8	20170106	10:20:48	ALOS-2 (WideSwath)	20170217	10:20:48	ALOS-2 (WideSwath)	Descending	39.04	*Right*	

*Time is in Coordinated Universal Time (UTC).

2 DATA AND METHODS

2.1 Seismic data and methods

The seismological analysis constrains the locations of the major events, provides the depth extent of the sequence and here, it is also used as an independent approach to validate the results of the geodetic inversions. To this end, seismic data were exploited to relocate the three major events examined, determine their source parameters (mechanism, depth, seismic moment) and calculate the distribution of slip onto the seismogenic fault plane, complementing InSAR modelling. Origin times and epicentre positions of the three main events presented here were determined by manual picking of *P* and *S* phases in the waveforms of regional stations, which are received in real-time by the Greek national networks. To calculate the focal mechanisms and slip distribution models of the three events, we used digital, three-component, full broad-band waveforms from stations at distances up to 250 km from the sources, located in Greece and Turkey (Fig. S1). The waveforms from the stations located in Greece were downloaded from the servers of the Hellenic Unified Seismological Network (HUSN), while those from the stations located in Turkey were downloaded from the eida-nodes maintained at ORFEUS (Observatories & Research Facilities for European Seismology). Prior to the inversion, the waveforms were baseline corrected, tapered, corrected for instrument response, converted to displacement, band-pass filtered (for Event 1 between 0.05 and 0.10 Hz; for Events 2 and 3 between 0.05 and 0.08 Hz) and resampled to 1 Hz. Synthetic Green's functions for all seismic applications herein were computed by the frequency–wave number method (Saikia 1994) and the 1-D velocity model of Novotný *et al.* (2001). This model (shown in Fig. S2), was originally developed for the region we study, and it has proved to be very effective in describing the regional wave propagation for the broader Aegean Sea region, also accounting for the characteristics of the waveforms in the low frequencies (e.g. Benetatos *et al.* 2004; Roumelioti *et al.* 2008; Kiratzi 2013, 2018 among others). The synthetic waveforms (Green's functions) were also bandpass filtered, exactly as the observed waveforms. At local to regional distances, the bandpass filtering we adopted, is commonly used, because it allows the use of relatively simple 1-D velocity models to describe the wave propagation from the source to the receiver (Dreger 2018). In practice, this narrow frequency band is a compromise between instrument limitations (shaping the low frequency limit) and the need to include long periods in the inversion, to limit the influence of the assumed velocity model on the inversion results.

The source models of the three events analysed, were computed using the Time-Domain Moment Tensor inversion method developed at the Berkeley Seismological Laboratory (Dreger 2002, 2003, 2018) and is widely used by seismological centres in Greece, Italy and Turkey. Inversions were run for different source depths from 2 to 15 km (with a 1 km step). The preferred solution was chosen, based on the peak value of the variance reduction (VR) which is a measure of the goodness of fit between synthetic (*s*) and observed (*d*) waveforms, and is quantified as:

$$VR = [1 - \left(\frac{\int [d(t) - s(t)]^2 dt}{\int d(t)^2 dt}\right)] \times 100 \qquad (1)$$

The slip distribution models of the three events analysed were computed using the finite fault approach of Dreger & Kaverina (2000) and Kaverina *et al.* (2002), based on the work of Hartzell & Heaton (1983). The method applied, described and documented in many other Aegean events (Kiratzi 2018 and references therein)

is based on a non-negative least-squares inversion. It requires simplifying assumptions including constant rupture velocity and dislocation rise time and poses slip positivity, seismic moment minimization and smoothing constraints during the inversion procedure. In our applications the fault model is parametrized as a rectangle, of 23 km length and of 14 km width, discretised into 322 subfaults of 1 km × 1 km. These dimensions are two to three times larger than those expected from empirical relations, in order to allow the slip to reach its preferable location on the fault. We also adopted a constant rupture velocity of 2.8 km s^{-1}, which is 0.8 Vs at the source depths of the events, and the rise time was set equal to 0.7 s.

2.2 InSAR data and methods

To optimize our geodetic inversions, we carefully selected the InSAR pairs and orbit availability, exploiting different satellites. Throughout this study, each acquisition date follows the naming convention of *yyyymmdd*, as shown in Table 1, which lists the radar acquisitions used. The data exploited are from Sentinel-1A and 1B and ALOS-2 satellites, which were launched recently (2014, 2016 and 2014, respectively) and are a courtesy of European Space Agency (ESA) and Japan Aerospace Exploration Agency (JAXA). Atmospheric corrections were applied using the Generic Atmospheric Correction Online Service for InSAR (GACOS) (Yu et al. 2017, 2018). The InSAR topographic contribution was removed using the Shuttle Radar Topography Mission SRTM –1 (resolution ∼30 m) Digital Elevation Model (e.g. Farr & Kobrick 2000).

The image processing was carried out with the SARscape software. For each pair of images, the master (pre-event) and slave (post-event) images were co-registered. Then, each master image was multiplied by the complex conjugate of the corresponding slave image, creating an interferogram. The latter was corrected in terms of orbits, atmosphere and topography. All interferograms were filtered using Goldstein filtering (Goldstein & Werner 1998). Interferometric fringes were then unwrapped with the minimum cost flow algorithm (Costantini 1998) and geocoded to get the line-of-sight (LoS) displacement maps used in modelling.

First, we identified the optimum SAR pairs to isolate the main seismic events (Table 1). Earthquake isolation through the choice of specific radar images depends mainly on the time and date of satellite acquisition and is not always guaranteed. For this reason, as will be shown below, a specific strategy was adopted for the source study of the events. In all the selected interferograms for inversion, there is at least one $M \geq 4.9$ event. Within the modelling procedure, we also assessed the parameters of possible orbital ramps affecting input data sets. Given the large amount of coherent pixels in the InSAR output and to avoid a computational overload, the displacement maps were down-sampled with a two-level density sampling grid: denser in the event proximity and coarser elsewhere.

The initial modelling is carried out by adopting the uniform slip in a homogenous and isotropic elastic half-space equation from Okada (1985); we start with a non-linear inversion scheme (Levenberg 1944; Marquardt 1963) to identify the fault parameters and mechanism (strike, dip, rake, slip, fault location, length, depth, width), possibly introducing seismological constraints from the focal mechanisms derived from the seismic waveform analysis. The optimization starts from a random fault configuration within given parameter ranges and it keeps minimizing the cost function Φ, based

on the weighted squares of the residuals between the observed and the predicted data:

$$\Phi = \frac{1}{N} \sum_i^N \frac{(\mathbf{d}_{i,obs} - \mathbf{d}_{i,mod})^2}{\sigma_i}, \qquad (2)$$

where $\mathbf{d}_{i,obs}$ and $\mathbf{d}_{i,mod}$ are the observed and modelled displacements of the ith data point and σ_i is the standard deviation of the Nth points (we assume σ_i to be the same for all points). The downhill algorithm is implemented with multiple restarts to guarantee the convergence to the global cost function minimum. After defining the fault geometry, we applied a linear inversion to obtain the slip distribution, extending the fault length and width to let the slip vanish to zero and subdividing the fault plane into subfaults of 1 km × 1 km. The linear inversion scheme we adopt (Atzori et al. 2009, 2012) is described by the equation:

$$\begin{bmatrix} \mathbf{d} \\ \mathbf{0} \end{bmatrix} = \begin{bmatrix} \mathrm{G} \\ \varepsilon \nabla^2 \end{bmatrix} \cdot \mathbf{m} \qquad (3)$$

where d is the InSAR data, $\mathbf{G}$ is the Green's functions matrix with the Laplacian operator ∇^2, tuned with the damping factor ε, obtained by trial-and-error (Menke 1989), to get a reliable slip distribution, described with the $\mathbf{m}$ vector of parameters. A further constrain of parameters positivity is adopted to prevent back-slip.

3 RESULTS

3.1 Seismicity-focal mechanisms

The swarm seismic activity at Biga peninsula is shown in Fig. 2. The focal mechanisms of the events contained in the satellite pairs, and calculated here by moment tensor inversion (no 1–3, Table 2), are numbered and denoted with the green beach-balls. Other available focal mechanisms (Table S1) of smaller-size events are indicated in black colour. Regarding the moment tensor inversion and the quality metrics, an indicative example (from Event 1) of the variance reduction (%VR) versus the focal depth, and the waveform fit between observed and synthetic waveforms, is shown in the supplement (Figs S3, S4, respectively). The focal mechanisms (Fig. 2a) indicate the prevalence of WNW–ESE almost pure normal faulting, in accordance with the regional stress field (Chatzipetros et al. 2013; Kiratzi 2014; 2018 and references therein). The seismicity is confined to the tip of Biga peninsula, almost beneath the village of Gülpinar, and extends offshore to the west. The along dip A–A' cross-section (Fig. 2b) shows that the swarm operated in the upper crust, at shallow depths (3–12 km). In conclusion, the sequence is attributed to the rupture of a normal fault dipping to the SW, in accordance with the most prominent faults in the region, as concluded by others as well (Ganas et al. 2018; Mesimeri et al. 2018).

3.2 Crustal deformation

With the pairs of 20170125_20170206 and 20170131_20170206, both from Sentinel-1, we managed to isolate Event 1 (Table 1, Fig. 3a). Deformation at Biga peninsula for the period 20170206_20170212 during which Event 3 occurred (Table 1) is shown in Fig. 3(b) and finally the interferogram 20170125_20170206 of Fig. 3(c) contains Events 1 and 2 together. The interferograms showing the cumulative deformation of all the events analysed in this study, are presented in Fig. 4, where both ascending and descending imagery was analysed from both

Table 2. Focal depths, seismic moments, Mo, and focal mechanisms of Events 1, 2 and 3 (Table 1) calculated from time–domain moment tensor inversion, using seismic waveforms from regional stations (see Fig. S1).

Event	Date YR/MM/DD	Origin Time UTC	Lat. ° N	Long. ° E	Depth (km)	M_w	Mo × 10e24 dyn-cm	Nodal plane 1 strike/dip/rake	Nodal plane 2 strike/dip/rake	P axis az°/pl°	T axis az°/pl°	Slip vector az°/pl°	VR %	DC %	Stations used
1	2017/02/06	03:51:40.7	39.5412	26.1102	6 (−2, + 1)	5.3	1.10	112 53 −91	294 37 −88	16 82	203 8	204 53	75	96	EZN, GADA, SMTH, CHOS, BLCB, KYMI, XOR
2	2017/02/06	10:58:02.2	39.5202	26.1058	8 (−2, + 0)	5.1	0.52	115 48 −99	308 43 −80	322 83	211 3	218 47	78	96	SIGR, CHOS, ERIK, ALN, RDO, SMTH, ALNA, KYMI. GONE
3	2017/02/07	02:24:04.0	39.5250	26.1208	8 (−1, + 0)	5.3	1.20	103 43 −93	288 47 −87	251 88	15 1	196 44	76	95	SIGR, GADA, SMTH, CHOS, BLCB, BALB, ALN, RDO, KYMI, PAIG

Slip vectors (azimuth/plunge is given) were calculated assuming that the fault plane is the south dipping nodal plane (Nodal Plane 1). VR per cent is the variance reduction of the inversion, which is a metric of the goodness of fit. DC per cent is the Double Couple percentage of the solution. Origin times and epicentres determined here by hand picking P and S phases in the waveforms from the regional stations. az: azimuth, pl: plunge.
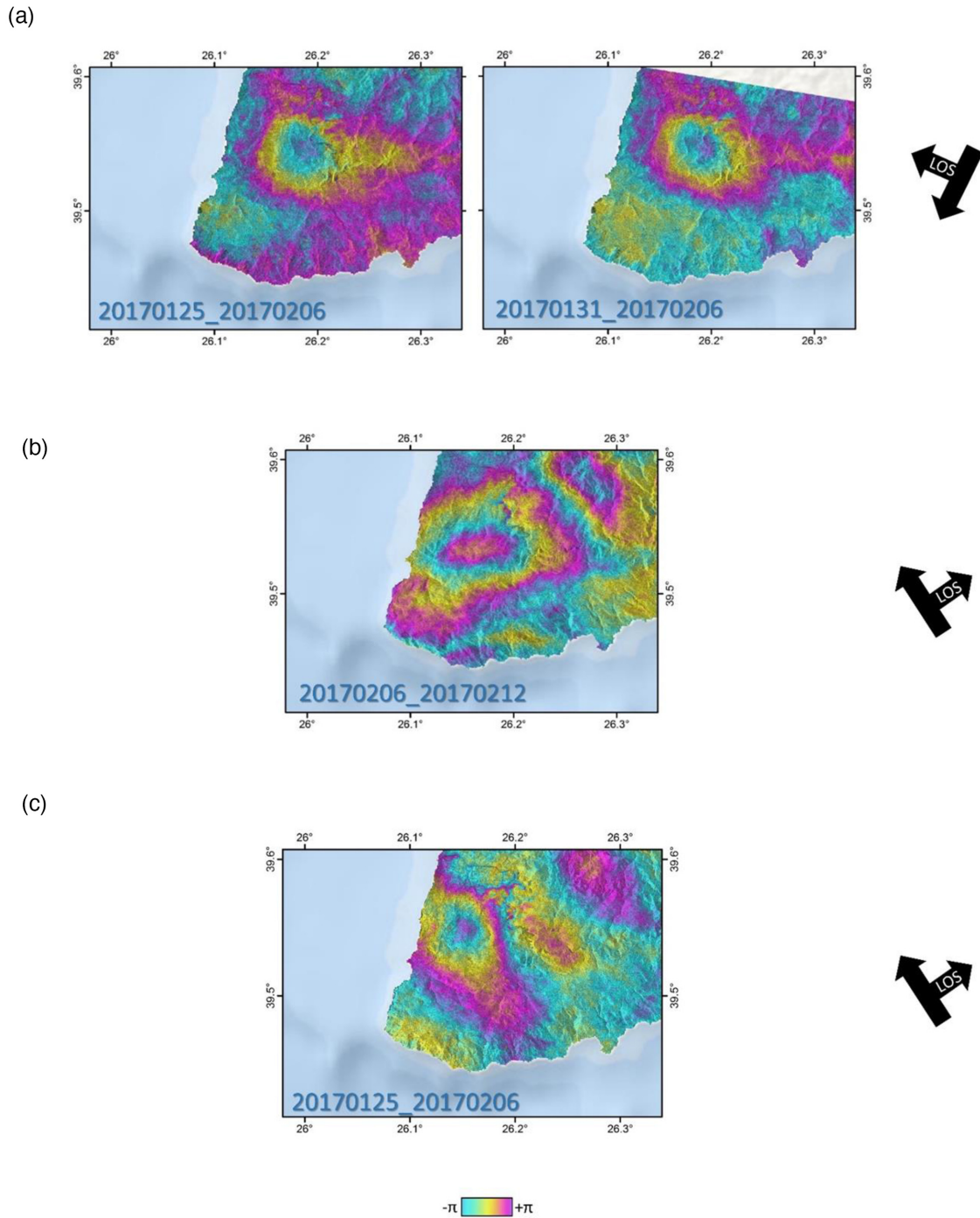
(a)

(b)

(c)

Figure 3. (a) Sentinel-1 Interferograms from the Descending pass showing the displacement caused by Event 1 (Table 1). (b) Sentinel-1 Ascending Interferogram showing the displacement caused by Event 3. (c) Sentinel-1 Ascending Interferogram of Events 1 and 2 (Table 1).

Sentinel-1 and ALOS-2 satellites. Detected cumulative in the LoS deformation is more than 7 cm.

3.3 InSAR source modelling

To initialize the InSAR non-linear inversion, where the range of possible values must be set for each fault parameter, we take into account the results of the seismic moment tensor inversion and in some cases we fixed a number of the parameters (Table S2) and

adopted the solutions as derived from the seismic data (Table 2). We used the 20170125_20170206 and 20170131_20170206 pairs to derive the source parameters for Event 1. After defining Event 1, we modelled the 20170206_20170212 interferogram to get Event 3 parameters; it should be noted that this InSAR pair contains also a fourth earthquake (12 February 2017, 13:48 M_w 5.1, Table S1). We tried to isolate it, however, we found that this particular event did not cause any detectable surface deformation signal (Fig. S5). Regarding Event 2, it was not possible to isolate its surface displacement just by choosing images with specific acquisition times; therefore,
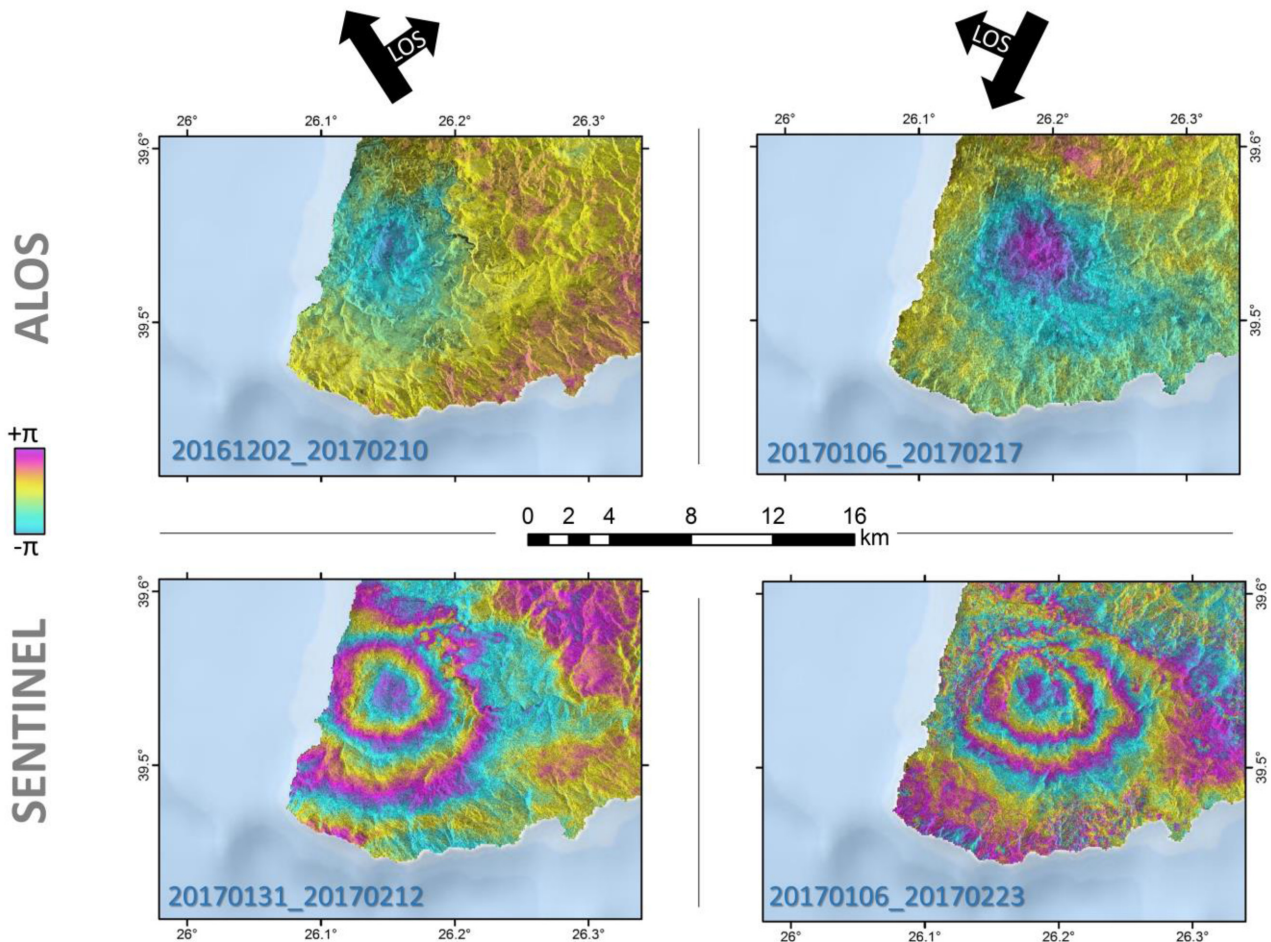
Figure 4. Fringe patterns from different satellites (Sentinel-1 and ALOS-2) and different viewing geometries (Left-hand panels: ascending, Right-hand panels: descending) that express the cumulative displacement caused by Events 1, 2 and 3 (Table 1).

we used the interferometric pair 20170125_20170206, containing the contribution of both Event 1 and Event 2 (Table 1), and by keeping fixed the previously defined source of Event 1, we inverted the residual signal to get the source parameters of Event 2.

Results of the non-linear inversions of all events and uncertainties are presented in the Supplementary material (Table S2 and Figs S6–S8). The rms values of each inversion can be found in Table S3, while observed and modelled interferograms are presented in Figs S9–S11.

3.4 Slip distribution onto the causative fault plane

Since an advantage of InSAR is its ability to constrain fault segmentation (Elliott *et al.* 2016), as a first step, we exploit the In-SAR modelling results from uniform slip models for Events 1–3 (Fig. S12), to investigate the segmentation. Although the three fault planes retrieved for Events 1–3 are not exactly coincided, the different positions and mechanisms can be attributed to the uncertainty, necessarily present in InSAR data, that propagated to the fault parameters (Table S2). Considering also that the Okada solution is a simplified description of a fault system, we conclude that the three events occurred on the same fault (or fault system). We then moved on to the slip distribution calculation, for InSAR and seismic waveforms inversion, adopting a strike 110°, dip 39° and rake -97° fault

plane, which are the mean values of those derived for Events 1–3. To linearly model geodetic data, we followed a stepwise procedure: first we estimated the slip distribution for Event 1, using interferograms No. 1 and No. 2 (Table 1); then we calculated the slip distribution of Event 3 using interferogram No. 3. For the linear inversion of Event 2, we followed the same strategy as the one adopted in the non-linear inversion, exploiting interferogram No. 4, setting as fixed the source of Event 1, which had already been assessed. Additionally, by using seismic waveforms and the inversion approach discussed in the methods, we also calculated the slip models for Events 1–3, using the same fault configuration to compare the source results of the two different approaches (crustal deformation and waveform).

Fig. 5 depicts the slip models from both data sets. For the geodetic modelling, the rms values are listed in Table S3, while the observed, modelled and the residuals are summarized in Fig. 6. For the seismic modelling, the fit of the synthetics to the observed waveforms, is presented in Figs S14–S16.

The following observations can be deduced from the slip distribution models (Fig. 5):

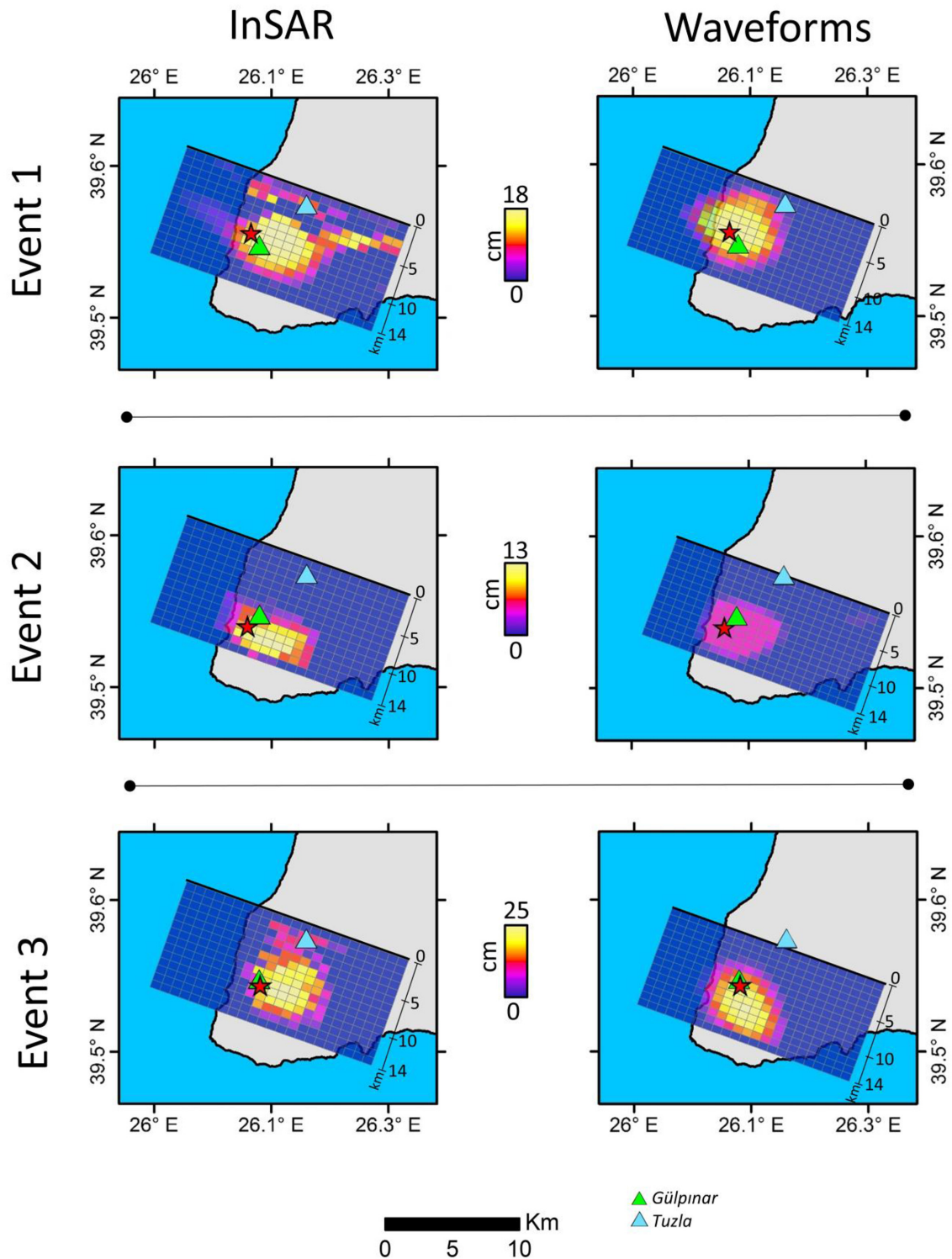(1) In all cases the slip is mainly confined to the mainland of Biga peninsula.

Figure 5. Slip distributions of Events 1, 2 and 3. Left-hand panel: from InSAR; Right-hand panel: from seismic data. The red star in each event denotes the hypocentre.

(2) The peak slip is in the range of 8–25 cm, and both approaches (InSAR and seismic) capture that the most energetic event was Event 3.

(3) In all cases, the town of Gülpınar is above the locus of peak slip and the town of Tuzla in close proximity.

(4) Both approaches predict that for Event 1, the slip extents to very shallow depths updip, almost reaching the surface. Both models also predict a striking proximity of the major slip to the town of Tuzla.
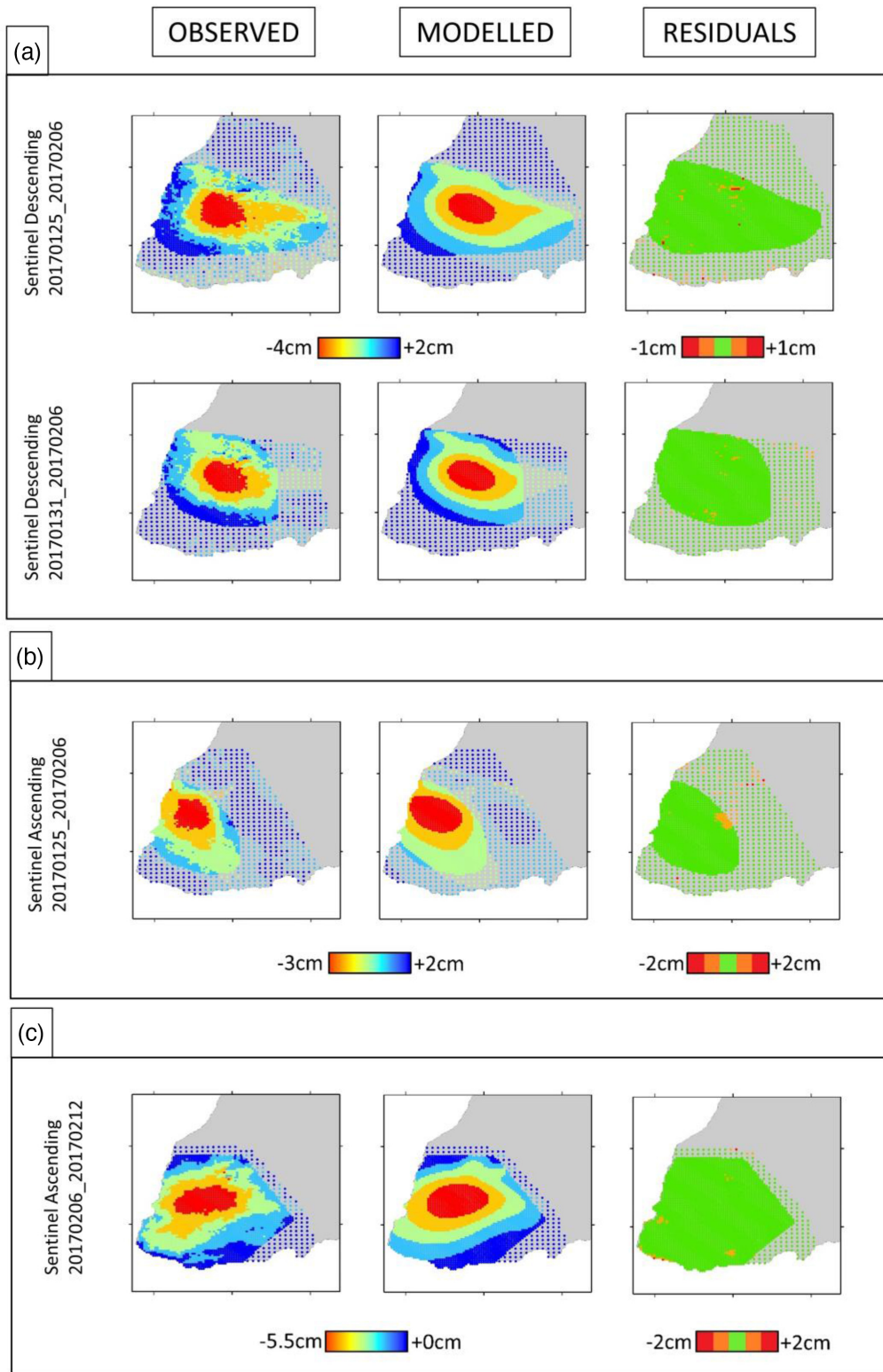
Figure 6. Observed, modelled and residuals of the slip distribution model of (a) Event 1, (b) Event 2 and (c) Event 3. Positive and negative signs mean, LoS shortening and lengthening, respectively.

(5) We note that the slip distributions for all the three events imaged through InSAR and seismic data, considering the different data and inversion schemes, are in good agreement.

3.5 Slip modelling validation and cumulative slip distribution

To further validate our InSAR modelling strategy and to demonstrate that we were in fact able to correctly separate the contributions of the three events, we carry out an independent modelling of an InSAR data set encompassing all the three events (Interferograms No 5–8, Table 1) and compare the retrieved slip distribution, with the total amount of the separate slip distributions of the three events (Slip distributions of: Event1 + Event2 + Event3) described in the previous section.

The addition of the separate slip distributions indicates a peak slip value of 44 cm at a depth of 5.6 km (Fig. 7a). The cumulative slip distribution of the three events (estimated onto the same mean fault surface), this time found from the inversion of the interferograms No. 5–8 in Table 1, indicates a peak slip value of 47 cm, located at a depth of 7.5 km (Fig. 7b). The high similarity of the two results, indicate that the sources' isolation strategy adopted in this study, has been successful. Observed modelled and residuals of the inversion of the cumulative interferograms are shown in Fig. 8 and rms values are found in Table 3.

4 ON-FAULT CFF CHANGES

A further objective is to investigate the possible interaction between the three major events, from the redistribution of stress that occurred on the causative fault. Failure is expected when there is an exceeding of cohesion of the combination of normal and shear stresses. Change in the Coulomb Failure Function (ΔCFF) is defined as:

$$\Delta CFF = \Delta\tau + \mu' \, \Delta\sigma, \tag{4}$$

where $\Delta\tau$ is the change in the shear stress, $\Delta\sigma$ is the change in the normal stress and μ' is the apparent coefficient friction (e.g. Reasenbeg & Simpson 1992; Harris 1998). Positive values of the results of eq. (4), favour failure of the faults, while the negative values suppress it. Poisson's ratio was 0.25 and the coefficient of friction was set to 0.4.

To carry out this analysis, we adopt the geodetic-based slip distribution models for each event and calculate the stress change using the formulation presented by Okada (1992). Fig. 9 shows the results of the Coulomb stress changes modelling, having as input, for the CFF calculation, first the source of Event 1 and then the sum of Event 1 and 2 slip distributions. In every estimate, we calculate the CFF adopting the rupture mechanism of the upcoming event, that is Event 2 for the first calculation and Event 3 for the second. In the figure, orange to red colors represent stress increase.

In Fig. 9, in the upper panel, it is shown that within the extent of the slip distribution of Event 2, positive values of ΔCFF (caused by Event 1) are estimated to exist. This implies that Event 2 could have been triggered from the stress changes of Event 1. The same criterion applies to the case of Event 3 (Fig. 9 lower panel); it is indicated that its failure could have been promoted from the areas of higher ΔCFF values, caused by both Events 1 and 2.

After investigating the ruptured fault CFF loading, we also examined the loading on the nearby Edremit fault, the most significant

tectonic structure in the region, this time adopting the cumulative slip that derived from the inversion of the cumulative interferograms (No. 5–8 in Table 1). We found that the Biga events only slightly loaded the Edremit fault, with maximum values of 0.056 MPa (Fig. S17).

5 CUMULATIVE SEISMIC AND GEODETIC MOMENT

An important implication for the seismic hazard of an area is the evaluation of seismic and geodetic release (e.g. Cheloni *et al.* 2017). Only recently, with the use of geodetic measurements, have we been able to have an insight into slow or aseismic processes. These type of activities can exist for example in active transform plate boundaries, where it has been found that they express aseismic slip (e.g. Lohman & McGuire 2007) and also volcanic regions (Segall *et al.* 2006). Among the most known 'silent' phenomena is the aseismic slow slip detected to occur at subduction zones around the globe (e.g. Wallace & Eberhart-Phillips 2013; Pritchard & Simons 2006). While usually swarms are associated with high pore fluid pressure in the crust (Hainzl 2004), other studies (Vidale & Shearer 2006) have suggested that aseismic processes may be one of their common features.

Motivated by the above, we used our moment tensor solution results together with those of Özden *et al.* (2018) and found the cumulative moment release of the earthquakes (during the timespan covered by our cumulative interferograms) to be equivalent to M_w 5.7. The cumulative slip distribution derived from the ALOS-2 and Sentinel-1 interferograms indicates a moment release (assuming rigidity $\mu = 30$ GPa) of M_w 5.8. The two values agree, which reveals that almost all of the deformation of the 2017 Biga swarm was seismic. However, from this swarm alone we cannot draw any conclusions whether the absence of aseismic transients characterizes the way of strain accumulation in this region. Future geodetic analyses and future seismic activity evaluation could potentially reveal whether this behaviour is typical of the area or whether there could be periods when strain is expressed aseismically

6 CONCLUSIONS

The 2017 Biga swarm created a signal strong enough to be detectable by the radar satellites and here we demonstrate a case in which InSAR is used to study swarm activity. Because of its high spatial resolution, InSAR is able to offer better constraints to epicentral positions with regard to waveform inversion. It can also clarify issues related to fault segmentation. Moreover, it offers insights into aseismic processes that cannot be observed solely by seismic measurements. The contribution from GPS campaigns is also valuable in such studies, but are more expensive and not always publically available, like in the case of free SAR data available to the scientific community.

The studied swarm in Biga peninsula was caused by the rupture of a normal fault, striking ~E–W and dipping (~40°) to SW, compatible with regional tectonics (Kiratzi 2018 and references therein). The entire sequence occurred at shallow focal depths in the upper crust. The slip distribution models obtained from geodetic and seismic data converge to show that the slip was confined mainly to a single compound patch, located underneath the town of Gülpınar and close to the town of Tuzla. The average slip for the three events is of the order of 15 cm and the peak slip in the
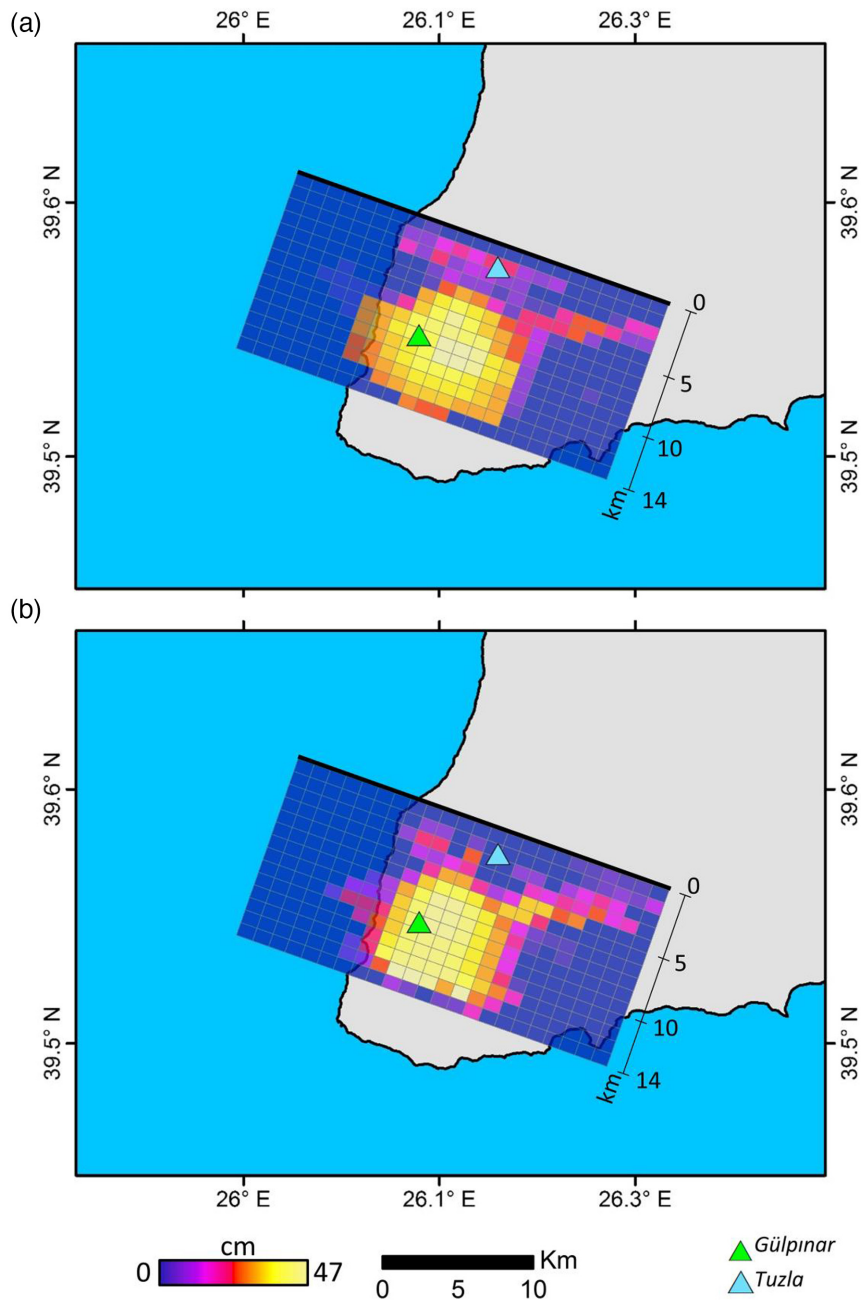
Figure 7. Cumulative slip distribution. (a) Cumulative slip distribution as derived from the addition of the three separate InSAR slip distributions presented in Fig. 5. (b) Cumulative slip distribution derived from the inversion of the displacement data of the interferograms shown in Fig. 4, that contain all the three events. The two results are in agreement, both in terms of slip amplitude and slip distribution.

range 8–25 cm. Event 1 shows greater complexity in its geodetic slip model, while Event 3 was more energetic in terms of peak slip values. The accumulated strain was released seismically with no aseismic transient. Our results of the isolated slip distributions were validated by an independent measurement, proving that InSAR is indeed capable of isolating slip distribution of swarm sources.

We demonstrate here that the Sentinel-1 family, together with the other available radar satellite installations, could potentially provide more opportunities to study these phenomena and even face the low temporal resolution of InSAR and define separate slip

distributions of a swarm's events by applying specific strategies. This additional input could improve the knowledge of each specific tectonic environment studied, but even on a larger scale, it can shed light on phenomena that occur during swarm activity and are not detectable with traditional instrumentation.

DATA AND SOURCES

Satellite data are from ESA and JAXA. The latter were obtained in the framework of the 4th Research Announcement
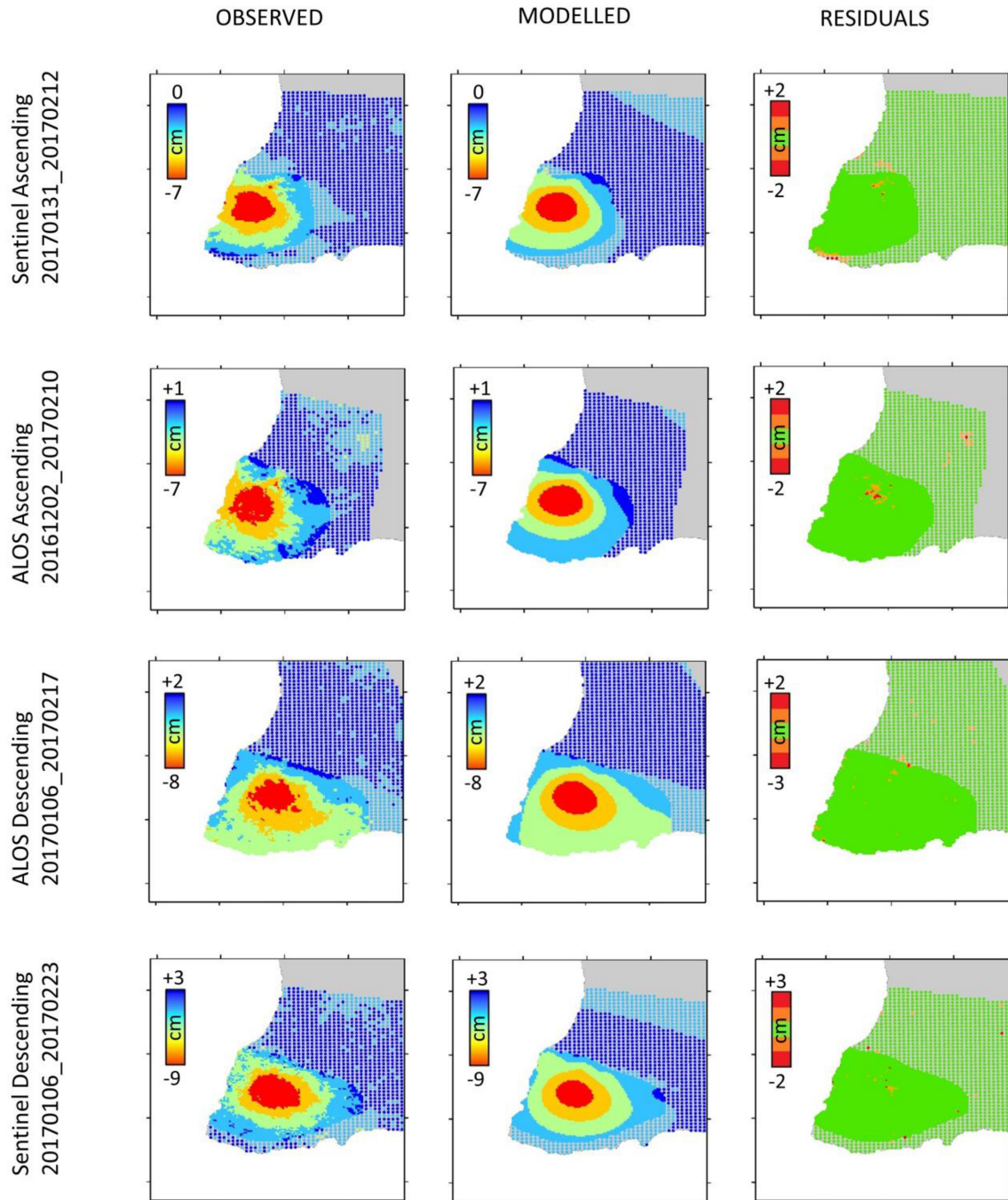
OBSERVED   MODELLED   RESIDUALS

Figure 8. Comparison between Observed and Modelled cumulative displacement according to the InSAR slip distribution model. Positive and negative signs mean, LoS shortening and lengthening, respectively.

Table 3. InSAR linear inversion results of the cumulative slip.

	Fault plane		Cumulative slip distribution from the cumulative interferograms (No 5–8, Table 1)	
Strike°	Dip°	Rake°	Peak Slip (cm)	Depth of peak slip (km)
110	39	-97	47	7.5
			RMS values (m)	
			Int. 20161202_20170210: 0.007	
			Int. 20170106_20170223: 0.007	
			Int. 20170106_20170217: 0.006	
			Int. 20170131_20170212: 0.005	
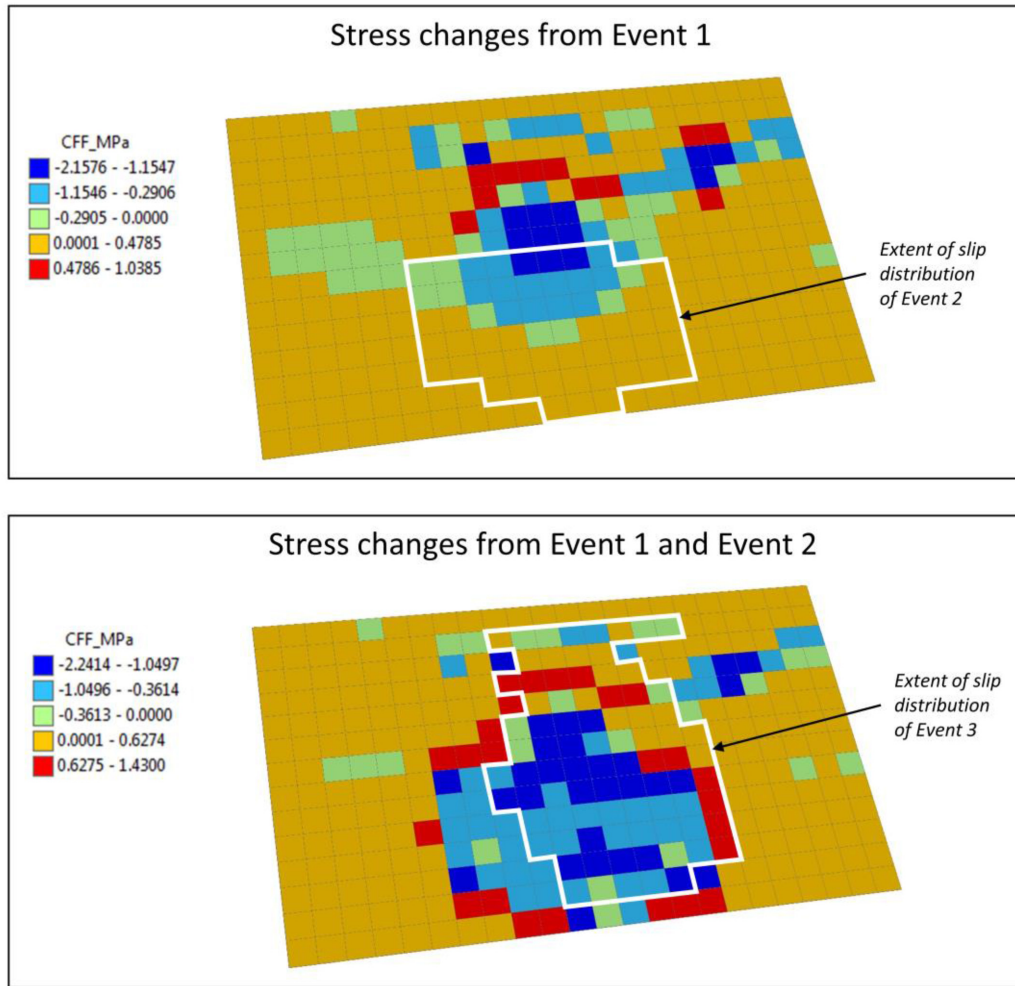
Figure 9. On-fault CFF changes based on the slip distribution models of each event. In the upper panel, receiver source is Event 2 and in the lower panel receiver source is Event 3. White polylines show in each case the slip distribution of the upcoming event.

REFERENCES

Altınok, Y., Alpar, B., Yaltırak, C., Pınar, A. & Özer, N., 2012. The earthquakes and related tsunamis of October 6, 1944 and March 7, 1867; NE Aegean Sea, *Nat. Hazards,* **60,** 3–25.

Ambraseys, N.N., 1988. Engineering seismology. Part I, *Earthq. Eng. Struct. Dyn.,* **17,** 1–105.

Atzori, S., Tolomei, C., Antonioli, A., Merryman Boncori, J.P., Bannister, S., Trasatti, E., Pasquali, P. & Salvi, S., 2012. The 2010–2011 Canterbury, New Zealand, seismic sequence: multiple source analysis from InSAR data and modeling, *J. geophys. Res.,* **117,** B08305, doi:10.1029/2012JB009178.

Atzori, S. *et al.*, 2009. Finite fault inversion of DInSAR coseismic displacement of the 2009 L'Aquila earthquake (central Italy), *Geophys. Res. Lett.,* **36,** L15305, doi:10.1029/ 2009GL039293.

Baba, A., Ates, Ö. & Deniz, O., 2008. The environmental and hydrogeochemical properties of the Tuzla-Kestanbol-Hidirlar geothermal sources, Turkey, in *Proceedings of the 30th Anniversary Workshop Engineering and Architectural Geothermal Training Programme,* Orkustofnun, Grensásvegur 9.

Baba, A., Demir, M.M., Koc, A.G. & Tugcu, C., 2015. Hydrogeological properties of hyper-saline geothermal brine andapplication of inhibiting siliceous scale via pH modification, *Geothermics,* **53,** 406–412.

Baba, A. & Ertekin, C., 2007. Determination of the source and age of the geothermal fluid and its effects on groundwater resources in Kestanbol (Çanakkale-Turkey), GQ07: securing groundwater quality in urban and industrial environments, in *Proceedings of the7th International Groundwater Quality Conference,* pp. 1–8, Fremantle, Western Australia.

Bell, J., Amelung, F. & Christopher, H., 2012. InSAR analysis of the 2008 Reno-Mogul earthquake swarm: evidence for westward migration of Walker Lane style dextral faulting, *Geophys. Res. Lett.,* **39,** L18306, doi:10.1029/2012GL052795.

Benetatos, C., Kiratzi, A., Kementzetzidou, K., Roumelioti, Z., Karakaisis, G., Scordilis, E., Latoussakis, I. & Drakatos, G., 2004. The Psachna (Evia Island) earthquake swarm of June 2003, *Bull. Geol. Soc. Greece,* **XXXVI**(3), 1379–1388.

Bulut, F., Havazlı, E., Yaltırak, C., Doğru, A., Sabuncu, A. & Özener, H., 2018. The 2017 Ayvacık earthquake sequence: a Listric fault activated beneath Tuzla/Çanakkale geothermal reservoir (Western Turkey) proceedings, in *Proceedings of the 43rd Workshop on Geothermal Reservoir Engineering Stanford University,* Stanford, California, February 12–14, 2018 SGP-TR-213.

Caputo, R. & Pavlides, S., 2013. The Greek Database of Seismogenic Sources (GreDaSS), Version 2.0.0: a compilation of potential seismogenic sources (Mw>5.5) in the Aegean region, doi:10.15160/unife/gredass/0200, [http://gredass.unife.it/.]

Chatzipetros, A., Kiratzi, A., Sboras, S., Zouros, N. & Pavlides, S., 2013. Active faulting in the north-eastern Aegean Sea Islands, *Tectonophysics,* **597–598,** 106–122.

Cheloni, D. *et al.*, 2017. Aseismic transient during the 2010–2014 seismic swarm: evidence for longer recurrence of M≥6.5 earthquakes in the Pollino gap (Southern Italy)?, *Sci. Rep.,* 57671, doi:10.1038/s41598-017-00649-z.

Costantini, M., 1998. A novel phase unwrapping method based on network programming, IEEE Trans, *Geosci. Remote Sens.,* **36**(3), 813–821.

Dixon, T.H., 1994. SAR interferometry and surface change detection, in *Proceedings of the Report of a Workshop,* Boulder, CO, USA.

Dreger, D.S., 2002. *Time-Domain Moment Tensor INVerse Code (TDMT_INVC) Version 1.1.,* pp. 18, Berkeley Seismological Laboratory.

Dreger, D.S., 2003. TDMT_INV: time domain seismic moment tensor INVersion, in *International Handbook of Earthquake and Engineering Seismology,* **Vol. B,** pp. 1627, eds Lee, W.H.K., Kanamori, H., Jennings, P.C. & Kisslinger, C., Academic Press.

Dreger, D.S., 2018. Berkeley seismic moment tensor method, uncertainty analysis, and study of non-double-couple seismic events, in *Moment Tensor Solutions,* pp. 75–92, ed. Amico, S.D., Springer Natural Hazards.

Dreger, D.S. & Kaverina, A., 2000. Seismic remote sensing for the earthquake source process and near-source strong shaking: a case study of the October 16, 1999 Hector Mine earthquake, *Geophys. Res. Lett.,* **27,** 1941–1944.

Elliott, J.R., Walters, R.J. & Wright, T.J., 2016. The role of space-based observation in understanding and responding to active tectonics and earthquakes, *Nat. Commun.,* **7,** doi:10.1038/ncomms13844.

Farr, T.G. & Kobrick, M., 2000. Shuttle radar topography mission produces a wealth of data, *EOS, Trans. Am. Geophys. Un.,* **81,** 583–585.

Ganas, A., Kourkouli, P., Briole, P., Moshou, A., Elias, P. & Parcharidis, I., 2018. Coseismic displacements from moderate-size earthquakes mapped by Sentinel-1 differential interferometry: the case of February 2017 Gulpinar earthquake sequence (Biga Peninsula, Turkey), *Remote Sens.,* **10,** 1089.

Goldstein, R.M. & Werner, C.L., 1998. Radar interferogram filtering for geophysical applications, *Geophys. Res. Lett.,* **25,** 4035–4038.

Hainzl, S., 2004. Seismicity patterns of earthquake swarms due to fluid intrusion and stress triggering, *Geophys. J. Int.,* **159,** 1090–1096.

Harris, R.A., 1998. Introduction to special section: stress triggers, stress shadows, and implications for seismic hazard, *J. geophys. Res.,* **103**(B10), 24 347–24 358.

Hartzell, S.H. & Heaton, T., 1983. Inversion of strong ground motion and teleseismic waveform data for the fault rupture history of the 1979 Imperial Valley, California, earthquake, *Bull. seism. Soc. Am.,* **73,** 1553–1583.

Kaverina, A., Dreger, D. & Price, E., 2002. The combined inversion of seismic and geodetic data for the source process of the 16 October 1999 Mw 7.1 Hector Mine, California, Earthquake, *Bull. seism. Soc. Am.,* **92,** 1266–1280.

Kiratzi, A., 2013. The January 2012 earthquake sequence in the Cretan Basin, south of the Hellenic Volcanic Arc: focal mechanisms, rupture directivity and slip models, *Tectonophysics,* **586,** 160–172.

Kiratzi, A., 2014. Mechanisms of earthquakes in Aegean, in *Encyclopedia of Earthquake Engineering,* pp. 1–22, eds Beer, M., Kougioumtzoglou, I.A., Patelli, E. & Siu-Kui Au, I., Springer.

Kiratzi, A., 2018. The 12 June 2017 Mw 6.3 Lesvos Island (Aegean Sea) earthquake: slip model and directivity estimated with finite-fault inversion, *Tectonophysics,* **724–725,** 1–10.

Kyriakopoulos, C., Chini, M., Bignami, C., Stramondo, S., Ganas, A., Kolligri, M. & Moshou, A. 2013. Monthly migration of a tectonic seismic swarm detected by DInSAR: southwest Peloponnese, Greece, *Geophys. J. Int.,* **194,** 1302–1309.

Levenberg, K., 1944. A method for the solution of certain problems in least squares, *Q. appl. Math.,* **2,** 164–168.

Livaoğlu, R., Timurağaoğlu, M.Ö., Serhatoğlu, C.S. & Döven, S., 2018. Damage during the 6–14 February 2017 Ayvacik (Çanakkale) earthquake swarm, *Nat. Hazards Earth Syst. Sci.,* **18,** 921–934.

Lohman, R.B. & McGuire, J.J., 2007. Earthquake swarms driven by aseismic creep in the Salton Trough, California, *J. geophys. Res.,* **112,** B04405, doi:10.1029/2006JB004596.

Marquardt, D., 1963. An algorithm for least-squares estimation of nonlinear parameters, *SIAM J. Appl. Math,* **11**(2), 431–441.

Massonnet, D., 1997. Satellite radar interferometry, *Sci. Am.,* **276**(2), 46–53.

Massonnet, D. & Feigl, K.L., 1998. Radar interferometry and its application to changes in the Earth's surface, *Rev. Geophys.,* **36,** 441–500.

Menke, W., 1989. *Geophysical Data Analysis: Discrete Inverse Theory,* Academic Press.

Mesimeri, M., Kourouklas, C., Papadimitriou, E., Karakostas, V. & Kementzetzidou, D., 2018. Analysis of microseismicity associated with the 2017 seismic swarm near the Aegean coast of NW Turkey, *Acta Geophys.,* 1–17

Mützenberg, S., 1997. Nature and origin of the thermal springs in the Tuzla area, Western Anatolia, Turkey, in *The Marmara Poly-Project,* pp. 301–317, eds Schindler, C. & Pfister, M., Vdf Hochschulverlag AG an der ETH, Zurich.

Novotný, O., Zahradník, J. & Tselentis, G.-A., 2001. North-Western Turkey earthquakes and the crustal structure inferred from surface waves observed in Western Greece, *Bull. seism. Soc. Am.,* **91,** 875–879.

Okada, Y., 1985. Surface deformation due to shear and tensile faults in a half-space, *Bull. seism. Soc. Am,* **75**(4), 1135–1154.

Okada, Y., 1992. Internal deformation due to shear and tensile faults in a half-space, *Bull. seism. Soc. Am.,* **82,** 1018–1040.

Paradisopoulou, P.M., Papadimitriou, E.E., Karakostas, V.G., Taymaz, T., Kilias, A. & Yolsal, S., 2010. Seismic Hazard Evaluation in Western Turkey as revealed by stress transfer and time-dependent probability calculations, *Pure appl. Geophys.,* **167,** 1013–1048.

Pavlides, S., Caputo, R., Sboras, S., Chatzipetros, A., Papathanasiou, G. & Valkaniotis, S., 2010. The Greek catalogue of active faults and database of seismogenic sources, *Bulletin of the Geological Society of Greece,* **XLIII (1),** 486–494.

Pritchard, M.E. & Simons, M., 2006. An aseismic slip pulse in northern Chile and along-strike variations in seismogenic behavior, *J. geophys. Res.,* **111,** B08405, doi:10.1029/2006JB004258.

Reasenberg, P. & Simpson, R., 1992. Response of regional seismicity to the static stress change produced by the loma Prieta Earthquake, *Science,* **255**(5052), 1687–1690.

Roumelioti, Z., Benetatos, C., Kiratzi, A. & Dreger, D., 2008. Near-real time moment tensors for earthquakes in Greece based on seismological data of the Hellenic Unified Seismological Network, in *Proceedings of the 3rd National Conference of Earthquake Engineering and Engineering Seismology,* Athens, 5–7 November, paper ID:1789.

Saikia, C.K., 1994. Modified frequency-wave-number algorithm for regional seismograms using Filon's quadrature–modeling of L(g) waves in eastern North America, *Geophys. J. Int.,* **118,** 142–158.

Sboras, S., 2012. The Greek Database of Seismogenic Sources: seismotectonic implications for North Greece, *PhD Thesis, University of Ferrara,,* 252.

Segall, P., Desmarais, E.K., Shelly, D., Miklius, A. & Cervelli, P., 2006. Earthquakes triggered by silent slip events on Kilauea volcano, Hawaii, *Nature,* **442,** 71–74.

Sözbilir, H., Sümer, O., Özkaymak, C., Uzel, B., Tayfun, G. & Semih, E., 2016. Kinematic analysis and palaeoseismology of the Edremit Fault Zone: evidence for past earthquakes in the southern branch of the North Anatolian Fault Zone, Biga Peninsula, NW Turkey, *Geodin. Acta,* **28**(4), 273–294.

Vidale, J.E. & Shearer, P.M., 2006. A survey of 71 earthquakes bursts across southern California: exploring the role of pore fluid pressure fluctuations and aseismic slip as drives, *J. geophys. Res.,* **111,** B05312, doi:10.1029/2005JB004034.

Wallace, L.M. & Eberhart-Phillips, D., 2013. Newly observed, deep slow slip events at the central Hikurangi margin, New Zealand: implications for downdip variability of slow slip and tremor, and relationship to seismic structure, *Geophys. Res. Lett.,* **40**(20), 5393–5398.

Wessel, P. & Smith, W.H.F., 1998. New improved version of the Generic Mapping Tools released, *EOS, Trans. Am. Geophys. Un.,* **79,** 579.

Yilmaz, Y. & Karacik, Z., 2001. Geology of the northern side of the Gulf of Edremit and its tectonic significance for the development of the Aegean grabens, *Geodin. Acta,* **14,** 31–43.

Yu, C., Li, Z. & Penna, N.T., 2018. Interferometric synthetic aperture radar atmospheric correction using a GPS-based iterative tropospheric decomposition model, *Remote Sens. Environ.,* **204,** 109–121.

Yu, C., Penna, N.T. & Li, Z., 2017. Generation of real-time mode high-resolution water vapor fields from GPS observations, *J. geophys. Res.: Atmos.,* **122,** 2008–2025

Zebker, H.A. & Goldstein, R.M., 1986. Topographic Mapping from interferometric synthetic aperture radar observations, *J. geophys. Res.,* **91,** 4993–4999.

Özalp, S., Emre, Ö. & Doğan, A., 2013. The segment structure of southern branch of the North Anatolian Fault and paleoseismological behaviour of the Gemlik Fault, NW Anatolia, *Gen. Direct. Min. Res. Explor. (MTA) Bull.,* **147,** 1–17.

Özden, S., Över, S., Poyraz, S.A., Güneş, Y. & Pınar, A., 2018. Tectonic implications of the 2017 Ayvacık (Çanakkale) earthquakes, Biga Peninsula, NW Turkey, *J. Asian Earth Sci.,* **154,** 125–141.

Şamilgil, E., 1966. Hydrogeological report of geothermal energy possibility survey of hot springs of Kestanbol and Tuzla village of Çanakkale, MTA, Ankara, report 4274.

Şanlıyüksel, D. & Baba, A., 2007. Hydrogeochemical and isotopic study of Kırkgeçit (Biga - Çanakkale) geothermal area, in *Proceedings of the 60th Geological Congress,* pp. 89–92, Ankara.

Şengör, A.M.C., 1979. The North Anatolian transform fault: Its age, offset and tectonic significance, *J. geol. Soc. Lond.,* **136,** 269–282.

Şengör, A.M.C., Tüysüz, O., İmren, C., Sakınç, M., Eyidoğan, H., Görür, G. & Le Pcihon, X., 2005. The geodinamica acta 293 North Anatolian Fault: a new look, *Annu. Rev. Earth planet. Sci.,* **33,** 37–112.

SUPPORTING INFORMATION

Supplementary data are available at *GJI* online.

Table S1. Available focal mechanisms for other earthquakes of the swarm, determined by moment tensor inversion (retrieved from the database of the Geodynamic Institute of Athens (http://bbnet.gein.noa.gr).

Table S2. InSAR results of non-linear inversions of Events 1, 2 and 3.

Table S3. Root mean square (rms) values of the non-linear and linear Inversions for Events 1, 2 and 3.

Figure S1. Location of the seismological stations (red squares), surrounding the tip of Biga Peninsula, whose records were used in the moment tensor and finite-fault slip inversions.

Figure S2. The velocity model (after Novotný *et al.* 2001) adopted in the calculation of the synthetic Green's functions, required for the (a) moment tensor inversions and (b) finite fault slip inversions, using seismic waveforms. Regarding the material properties, we used values for the quality factor for the P and S waves equal to $Qp = 300$ and $Qs = 150$, respectively for all layers above the half-space, and $Qp = 1000$ and $Qs = 500$ for the half-space. The densities (in $gr\,cm^{-3}$) for the different layers were taken equal to: $[0–1\ km] = 2.16$; $[1–2\ km] = 2.56$; $[2–5\ km] = 2.80$; $[5–16\ km] = 2.94$; $[16–33\ km] = 2.98$ and equal to 3.36 for the half-space.

Figure S3. An example of a grid search for the best fitting focal depth for Event 1, during the moment tensor inversion, based on the variance reduction (%VR). The best solution is easy to depict, but it is noted that for very shallow depths and for larger than ∼8 km, the focal mechanisms tend to become strike-slip. This is quite common during moment tensor inversions for the broader western Anatolia. In particular, there is usually a limited depth range, when the solutions are stable—mainly pure normal faulting—with high variance reduction, but for shallower and deeper depths, the fit deteriorates and the solutions tend to become strike-slip. This is observed to the waveform fits as published by other agencies as well, using different inversion codes and velocity models. In other words, the selection of the best solution (a pure normal versus a strike-slip) sometimes is subjectable. This can be attributed to the transtentional stress regime, or to inaccurate Green's functions, or both.

Figure S4. An example of waveform fit between observed (black continuous lines) with synthetics (red dashed lines) for the moment tensor solution of Event 1.

Figure S5. DInSAR result of the 4th seismic event, which indicates a lack of a significant deformation signal.

Figure S6. Trade-offs and uncertainties of source parameters for Event 1. For the estimation of uncertainties, interferograms with realistic noise were simulated and were subsequently inverted for the source parameters. The results were compared with the optimal values found by our preferred solution. Scattered plots show the trade-offs between the parameters. Red points indicate the optimal values. The bottom histograms are the *a postetiori* probability distributions of the parameters. Black curves are showing the Gaussian fit.

Figure S7. Trade-offs and uncertainties of source parameters of Event 2.

Figure S8. Trade-offs and uncertainties of source parameters of Event 3.

Figure S9. Observed, modelled and residuals of the InSAR non-linear inversion of 20170125_20170206 and 20170131_20170206

for the source of Event 1. Positive and negative signs mean, LoS shortening and lengthening, respectively.

Figure S10. Observed, modelled and residuals of the InSAR non-linear Inversion for the source of Event 2. Positive and negative signs mean, LoS shortening and lengthening, respectively.

Figure S11. Observed, modelled and residuals of the InSAR non-linear inversion of 20170206_20170212 for the source of Event 3. Positive and negative signs mean, LoS shortening and lengthening, respectively.

Figure S12. The non-linear solutions of Events 1, 2 and 3 (a) planar view, (b) 3-D view.

Figure S13. Slip distribution uncertainties. For practical reasons, we only show the diagonal values of the full variance–covariance matrix of the model parameters. The distributed uncertainty gives a qualitative idea of the parameter uncertainty, since off-diagonal values (not shown) do not allow them to vary independently (i.e. for the ith patch, the slip value s_i is not strictly $s_i \pm \sigma_i$).

Figure S14. Predicted (dashed lines) displacement broad band waveforms, which were calculated using forward modelling and the derived slip models (for Events 1 to 3) and their fit to the observed (straight lines). The station code and the corresponding component are shown above each plot. Component waveforms flagged with an asterisk were not included in the inversion and are only shown here for comparison.

Figure S15. As in Fig. S14 for Event 2. Component waveforms flagged with an asterisk were not included in the inversion and are only shown here for comparison.

Figure S16. As in Fig. S14 for Event 3. Component waveforms flagged with an asterisk were not included in the inversion and are only shown here for comparison.

Figure S17. Model that investigates the potential interaction of the 2017 swarm with Edremit fault in terms of Coulomb stress changes. Poisson's ratio was 0.25 and coefficient of friction was set to 0.4. The geometric parameters of the receiver fault of Edremit was based on the 1944 event, strike: 74°/dip: 46°/rake: –114° (e.g. Paradeisopoulou *et al.* 2010). Results do not appear to indicate a significant stress loading.

Please note: Oxford University Press is not responsible for the content or functionality of any supporting materials supplied by the authors. Any queries (other than missing material) should be directed to the corresponding author for the article.